Theoretical Determination of Band Edge Alignments at the Water–CuInS$_2$(112) Semiconductor Interface

Thomas P. Senftle[†] and Emily A. Carter*[,‡]

[†]Department of Mechanical and Aerospace Engineering and [‡]School of Engineering and Applied Science, Princeton University, Princeton, New Jersey 08544-5263, United States

S *Supporting Information*

ABSTRACT: Knowledge of a semiconductor electrode's band edge alignment is essential for optimizing processes that occur at the semiconductor/electrolyte interface. Photocatalytic processes are particularly sensitive to such alignments, as they govern the transfer of photoexcited electrons or holes from the surface to reactants in the electrolyte solution. Reconstructions of a semiconductor surface during operation, as well as its interaction with the electrolyte solution, must be considered when determining band edge alignment. Here, we employ density functional theory + *U* theory to assess the stability of reconstructed CuInS$_2$ surfaces, a system which has shown promise for the active and selective photoelectrocatalytic reduction of CO$_2$ to CH$_3$OH. Using many-body Green's function theory combined with calculations of surface work functions, we determine band edge positions of explicitly solvated, reconstructed CuInS$_2$ surfaces. We find that there is a linear relationship between band edge position and net surface dipole, with the most stable solvent/surface structures tending to minimize this dipole because of generally weak interactions between the surface and solvating water molecules. We predict a conduction band minimum (CBM) of the solvated, reconstructed CuInS$_2$ surface of −2.44 eV vs vacuum at the zero-dipole intercept of the dipole/CBM trendline, in reasonable agreement with the experimentally reported CBM position at −2.64 eV vs vacuum. This methodology offers a simplified approach for approximating the band edge positions at complex semiconductor/electrolyte interfaces.
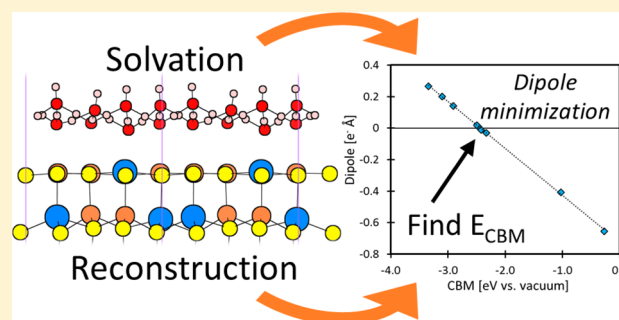
1. INTRODUCTION

Understanding the structure and composition of photoelectrode surfaces, as well as their interaction with the aqueous electrolyte, is essential for predicting band edge alignments that dictate overall electrode performance.[1,2] This alignment determines the thermodynamic feasibility of reaction steps induced by photoexcitation. As such, the ability to predict the impact of solvation on the band edge position is essential for improving photoelectrode design. Accurate prediction of the band edge position of a solvated semiconductor surface is challenging due to the complexity of the H$_2$O/surface interface, where dipoles can form readily in response to surface reconstruction and the adsorption of charged species from the electrolyte.[3] Previous approaches to this problem have employed ab initio molecular dynamics (AIMD) simulations to sample the dynamic interaction between solvating water molecules and the electrode surface.[2,4−6] Such calculations, while accurate, do require significant computational resources, which become prohibitive in studies seeking to screen multiple semiconductor materials. As an alternative, here we present a simplified approach for modeling the average effect of solvation on a semiconductor's band edge position, which can be used as a first approximation for determining the band edge alignment of many semiconductor/electrolyte systems.

Experimental reports have demonstrated that CuInS$_2$(112) photoelectrodes[7−9] can actively (only 20 mV overpotential) and selectively (97% Faradaic efficiency) reduce CO$_2$ to methanol in the presence of a pyridine cocatalyst. We employ density functional theory (DFT) + *U* and many-body Green's function calculations to better understand this promising system and to identify stable reconstructions of the CuInS$_2$(112) surface within the formalism of atomistic thermodynamics, following procedures described by Moll et al.[10] for applying atomistic thermodynamics to predict reconstructions of semiconductor surfaces. Our results demonstrate that Cu$_{In}$ antisite defects are highly stable on the CuInS$_2$(112) surface, where such defects eliminate unstable dangling bonds present in the stoichiometric termination of the (112) surface. Having identified the most favorable reconstructions, we then investigate the interaction between the reconstructed surface and solvating H$_2$O molecules. We utilize models of the solvated, reconstructed surface to determine the

impact of solvation on the band edge positions of the semiconductor. We find that there is a linear relationship between band edge position and net surface dipole, where the latter is affected by both the concentration of surface defects and the orientation of the solvating water layer. The interaction between water and the surface is weak, which allows the water layer to freely orient itself counter to the surface dipole. This leads to a net zero dipole in the most stable geometries of the surface/solution interface. We use this principle of dipole minimization in conjunction with the linear relationship between dipole and band edge position to determine the band edge alignment of the solvated, reconstructed $CuInS_2$ surface. We validate this approach through comparisons to experimental measurements.

2. METHODS

DFT-based calculations were completed with the Vienna ab initio simulation package (VASP 5.3.2).[11] The Perdew−Burke−Ernzerhof (PBE) generalized gradient approximation of the exchange-correlation functional was employed.[12] The Dudarev formulation[13] of the on-site effective U correction was used to treat spurious delocalization of 4d states on Cu(I) sites, where we employ U_{eff} = 3.6 eV, in accordance with a value derived previously[14] employing a fully ab initio methodology developed by Mosey et al.[15] We also applied Grimme's empirical dispersion correction,[16] as such corrections will be essential in subsequent studies investigating the physisorption interaction between CO_2 and surface models derived in this work. All nuclei and frozen core electrons were represented with the projector-augmented-wave (PAW) approximation[17] utilizing VASP default potentials.[18] The following electrons were treated self-consistently for each atom type: $Cu-3d^{10}4s^1$, $In-4d^{10}5s^25p^1$, $S-3s^23p^4$, $O-2s^22p^4$, and $H-1s^1$. All calculations were spin-polarized, and plane-wave basis sets were expanded up to an 800 eV kinetic energy cutoff. The Brillouin zone was sampled with the Monkhorst−Pack (MP)[19] formulation used to generate 5 × 5 × 1 and 2 × 2 × 1 spacing for (2 × 2) and (4 × 4) periodic slab unit cells, respectively. The Gaussian smearing method was used to integrate the Brillouin zone, with a smearing width of 0.05 eV. Periodic slab images perpendicular to the surface were separated by a vacuum layer of at least 15 Å, where a surface dipole correction was included to counter slab−slab interactions. These parameters converged the total energy to within 1 meV per formula unit.

Geometry optimizations resulted in force convergence to within 0.01 eV Å^{-1}, and energy minima were confirmed with frequency analyses to ensure that no imaginary frequencies were present. Imaginary frequencies persisted in some structures involving multiple adsorbed water molecules despite attempts to eliminate imaginary modes using a mode-following procedure with a tighter force convergence criterion (0.005 eV Å^{-1}). In all such cases, the recalcitrant frequencies were less than 50 cm^{-1} and are reported in the Supporting Information (SI). Since the identified water structures aim to sample a dynamic water layer, which will generally not reside at local energy minima, the presence of these imaginary frequencies will not impact any conclusions drawn herein. We also conducted an AIMD simulation of explicit solvating water molecules over the $CuInS_2$ surface to further sample structures in the dynamic water layer. This simulation employed the (2 × 2) periodic surface model described above at 300 K with a 0.5 fs time step. The MP k-point sampling and kinetic energy cutoff were reduced to 3 × 3 × 1 and 600 eV, respectively, for computational efficiency. Free energies were derived using statistical mechanical expressions for the ideal gas, rigid rotor, and harmonic oscillator to determine translational, rotational, and vibrational contributions, respectively. Translational and rotational contributions were omitted in all calculations featuring an extended surface, which has no translational or rotational degrees of freedom.

The intrinsic band gap of $CuInS_2$ was determined with a non-self-consistent many-body Green's function (G_0W_0)[20] calculation of the quasi-particle gap (E_g) in a primitive bulk $CuInS_2$ unit cell containing two Cu atoms, two In atoms, and four S atoms. The ground-state electron density for this calculation was determined with the HSE06 functional,[21] as the PBE + U functional significantly underestimates the band gap of $CuInS_2$. The HSE06 calculation employed a 6 × 6 × 6 Γ-point-centered k-mesh, 600 eV kinetic energy cutoff, and 96 bands. The subsequent G_0W_0 calculation contained 64 frequency points and yielded a quasi-particle gap of E_g = 1.31 eV, in reasonable agreement with the experimental value[7] of E_g = 1.53 eV. The reported magnitude of the intrinsic band gap of bulk $CuInS_2$ obtained via the G_0W_0 approach is converged to within 0.03 eV with respect to the number of empty states considered in the calculation (Figure S1).

All reported band edge positions were calculated with a methodology developed by Toroker et al.[22] In this method, PBE + U theory is used to determine the work function of a periodic slab model of the electrode surface (i.e., the band gap center (E_{BGC}) of the semiconductor relative to vacuum), and the G_0W_0 band gap of bulk $CuInS_2$ $(E_g$ = 1.31 eV) is used to determine the conduction band minimum (CBM) and valence band maximum (VBM) relative to E_{BGC}. This approach is motivated by a theorem presented by Perdew and Levy,[23] which demonstrates that DFT, even with an exact XC functional, can only yield a lower limit for the absolute position of the VBM. This theorem, however, demonstrates that the absolute position of E_{BGC} derived from DFT is formally exact. Moreover, eigenvalue gaps derived from DFT are not equivalent to energy gaps measured with optical or photoemission/inverse-photoemission (PES/IPES) experiments, which is an artifact of the incorrect derivative discontinuity in the XC functional. Hence, DFT is used to determine only E_{BGC} of the surface slab models employed in this study, and not the position of the VBM and CBM. On the other hand, the energy gap obtained with G_0W_0 corresponds to the difference in ionization potential and electron affinity of the material, which can be directly compared to experimental PES/IPES gaps. Thus, the positions of the VBM and CBM are derived with the relations: $E_{CBM} = E_{BGC} + 1/2E_g$ and $E_{VBM} = E_{BGC} − 1/2E_g$, where E_{BGC} is calculated with respect to vacuum using slab models of the $CuInS_2$ surfaces and E_g is calculated from bulk $CuInS_2$.

Simplifying idealizations inherent to this approach must be considered when drawing empirical conclusions regarding the comparison of calculated band edge positions and those measured experimentally. The employed formulas for adding or subtracting the G_0W_0 corrections of $1/2E_g$ to E_{BGC} assume that the semiconductor is not doped, as the Fermi level of p-type or n-type semiconductors will be shifted below or above E_{BGC}, respectively. This shift would break the assumed symmetric application of a $1/2E_g$ correction to derive the band edges relative to E_{BGC}. The Fermi level can be also shift away from E_{BGC} if there is a significant asymmetry in the number of states at the CBM and VBM. Finally, it is assumed that photoexcited electrons are predominantly generated in the bulk of the material, and therefore, E_g is calculated with a bulk model of $CuInS_2$, as opposed to a surface model.

A periodic slab model of the chalcopyrite $CuInS_2(112)$ surface was built with a (2 × 2) expansion of the optimized bulk unit cell and consisted of five $CuInS_2$ bilayers. Each layer contained two Cu atoms, two In atoms, and four S atoms, with the three bottom layers fixed in their bulk lattice positions during all optimizations. A (4 × 4) supercell with three bilayers and one fixed layer was employed to test low adsorbate coverages and defect concentrations. Surface energies varied by less than 0.5 meV Å^{-2} (∼0.01 J m^{-2}) between the three- and five-layer slab models, demonstrating that our results are converged with respect to slab thickness. To verify that the position of the band gap center derived with the five-layer slab model is converged with respect with slab thickness, we additionally calculated the position of the band gap center employing a seven-layer slab model of the surface. This calculation demonstrates that the position of the band gap center relative to vacuum is converged to within 0.05 eV with respect to the thickness of the slab model (Figure S2). Dangling bonds on the reverse side of the slab were saturated by pseudohydrogens with core charges (Z) of Z = +1/4e and Z = +3/4e when taking the lattice position of Cu and In atoms, respectively. Saturators were initially placed in the chalcopyrite crystallographic position immediately below the bottom surface layer, and saturator−slab bond lengths were

subsequently relaxed to an equilibrium position. This methodology for saturating dangling bonds in semiconductor surfaces was proven reliable in previous publications.[24,25] The resulting stoichiometric surface model is shown in Figure 1, and all atomic coordinates are provided in the SI.
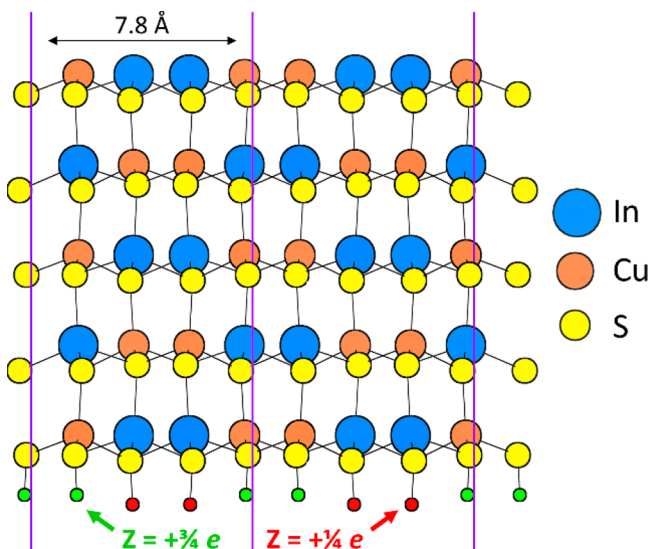

Figure 1. Side view of the five bilayer (2×2)-CuInS$_2$(112) slab model.

3. RESULTS AND DISCUSSION

3.1. CuInS$_2$(112) Surface Reconstructions. The polar CuInS$_2$(112) surface is prone to reconstructions that eliminate high-energy states associated with dangling bonds present in the stoichiometric surface.[26] Such reconstructions can lead to the formation of significant surface dipoles, which in turn affect the alignment of the semiconductor's conduction band (CB) and valence band (VB) edges. Furthermore, reconstructions lead to unique adsorption sites and it therefore is essential to identify reconstructions that are stable when the surface is in equilibrium with the electrolyte solution. The presence of high-energy states related to dangling bonds on the CuInS$_2$(112) surface are demonstrated by the density of states (DOS) analysis reported in Figure 2. The stoichiometric termination of the surface leaves dangling bonds associated with Cu and In atoms (Figure 2a,b), which create occupied CB states below the Fermi level (Figure 2c). Such states are evident in the DOS of the stoichiometric surface regardless of how spin restrictions are imposed in the electronic structure calculation, as excess electrons are forced to occupy high energy states associated with the CB. Hence, stable surface reconstructions will eliminate the high-energy states evident in the DOS of the stoichiometric surface (Figure 2c).

Favorable reconstructions can be identified using electron counting (EC) rules[27] to predict surface structures that will eliminate dangling bonds present in the stoichiometric surface, as previously demonstrated for polar GaAs(111), GaP(111), and CdTe(111) surfaces.[10,27,28] EC rules assign a fractional number of electrons contributed to a bond by each atom type, based on the valence of atoms involved in the bond. In the chalcopyrite structure of CuInS$_2$, each Cu or In atom forms four bonds to neighboring S atoms. Each In atom contributes three valence electrons to a total of four bonds; we therefore assign 3/4 e$^-$ to each dangling In bond at the surface. Similarly,
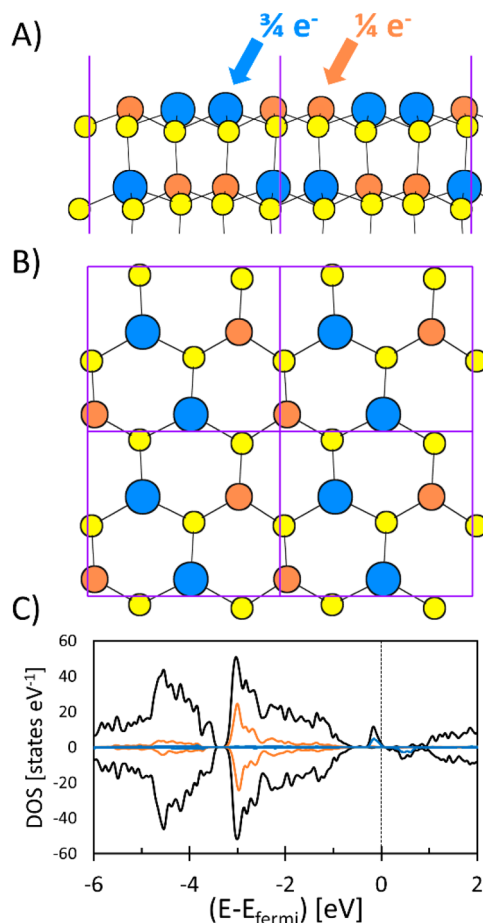

Figure 2. (a) Side and (b) top views of the stoichiometric CuInS$_2$(112) surface. (c) Total DOS (black) and partial (P)DOS, where orange data correspond to surface Cu atoms and blue data correspond to surface In atoms. Positive and negative DOS refer to majority and minority spin manifolds, respectively. The vertical dotted line corresponds to the Fermi level. The (2×2) unit cell is denoted with purple lines, and Cu, In, or S atoms are represented by orange, blue, or yellow circles, respectively. For clarity, only surface atoms are shown in (b).

each Cu atom contributes one valence electron to a total of four bonds; we therefore assign 1/4 e$^-$ to each dangling Cu bond. These assigned values can be used to determine the number of electrons per surface cell that need to be removed by a reconstruction to yield a stable, semiconducting surface. A (2×2)-CuInS$_2$(112) supercell exposes two dangling In bonds and two dangling Cu bonds; two electrons therefore occupy high-energy states near the CBM, as can be seen in Figure 2c. These rules also ensure that all electrons associated with dangling bonds created by the truncation of the stoichiometric surface can be stabilized by forming a lone pair on a surface anion or by forming a dative bond on a surface cation.

There are multiple reconstructions of the (2×2) surface that can achieve the two-electron oxidation required to form a stable surface, as summarized in Figure 3. The simplest reconstruction requires the adsorption of one additional S atom in the (2×2) cell, where the surface dangling bonds are saturated by forming new bonds to the S adatom (Figure 3a, designated as CuInS$_2$(112)-S$_{ad}$). The In–In bridge site shown in the figure was determined to be the most favorable adsorption site, where all other bridge, atop, and hollow sites were also considered. A surface Cu$_{In}$ antisite defect (in which one surface In is replaced
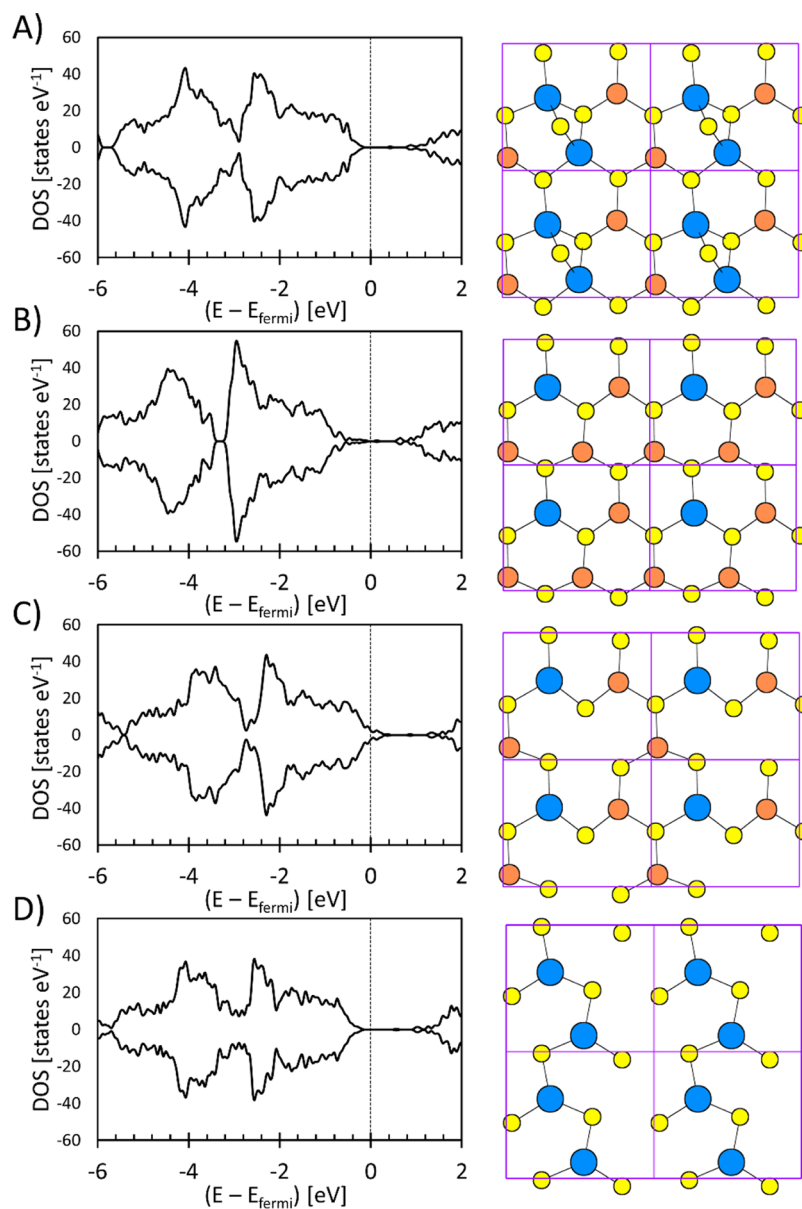
Figure 3. Total DOS (left) and top view (right) of the (2×2)-$CuInS_2$(112) surface cell with (a) one S adatom, (b) one Cu_{In} antisite defect, (c) one In vacancy, and (d) two Cu vacancies. The vertical dotted line corresponds to the Fermi level. The unit cell is denoted with purple lines, and Cu, In, or S atoms are represented by orange, blue, or yellow circles, respectively. Only surface atoms are shown for clarity.

by Cu per (2×2) cell) also achieves the required oxidation; removal of a neutral In atom results in a three-electron oxidation and addition of a neutral Cu atom leads to a one-electron reduction, thus yielding a net two-electron oxidation of the surface (Figure 3b, designated as $CuInS_2$(112)-Cu_{In}). A single In vacancy per (2×2) cell results in a three-electron oxidation, which is accommodated by the formation of one surface Cu^{2+} state (Figure 3c, designated as $CuInS_2$(112)-In_{vac}). This leads to a semiconducting surface with p-type character, as demonstrated by the position of the Fermi level in this surface's DOS. Finally, a single Cu vacancy per (2×2) cell results in a one-electron oxidation, and therefore is not sufficient to shift all high-energy CB states above the Fermi level. Rather, two Cu vacancies are required to achieve the necessary two-electron oxidation of the surface (Figure 3d, designated as $CuInS_2$(112)-$2Cu_{vac}$). As is clear from the DOS in Figure 3, all four reconstructions produce stable, semiconducting surfaces with

no dangling bond states in the gap. Figure 3c demonstrates the presence of hole states in the VB of the $CuInS_2$(112)-In_{vac} surface, where the In vacancy removed three electrons, creating a p-type semiconducting surface, as opposed to the two electrons required to form a surface that is an intrinsic semiconductor (as is evident in the DOS of all other surfaces shown in the figure). Atomic coordinates of optimized surface reconstructions are provided in the SI.

We employ the formalism of atomistic thermodynamics to identify which of the feasible reconstructions identified with EC rules is the most stable as a function of synthesis and operating conditions. Here, we follow the methodology presented by Moll et al.[10] for identifying reconstructions of GaAs surfaces, and later applied separately by Jaffe and Zunger[29] and by Zhang and Wei[30] to identify reconstructions of the related $CuInSe_2$(112) surface. The free energy of a $CuInS_2$ surface

reconstruction is calculated relative to the chemical potential of its constituent atoms with the equation:

$$G_{\text{surface}}(\mu_{\text{Cu}}, \mu_{\text{In}}, \mu_{\text{S}})$$
$$= E_{\text{surface}} - N_{\text{surface}}^{\text{Cu}} \cdot \mu_{\text{Cu}} - N_{\text{surface}}^{In} \cdot \mu_{\text{In}} - N_{\text{surface}}^{S} \cdot \mu_{\text{S}} \quad (1)$$

where G_{surface} is the free energy of the reconstructed surface calculated as a function of the chemical potential of Cu, In, and S (μ_{Cu}, μ_{In}, and μ_{S}, respectively); E_{surface} is the total DFT + U energy of the slab model; and $N_{\text{surface}}^{\text{Cu}}$, $N_{\text{surface}}^{\text{In}}$, and N_{surface}^{S} are the respective total number of Cu, In, and S atoms in the slab model. The free energy difference between surface reconstructions with varying numbers of each atom type can be determined directly from eq 1:

$$\Delta G_{1 \to 2}(\mu_{\text{Cu}}, \mu_{\text{In}}, \mu_{\text{S}})$$
$$= \Delta E_{1 \to 2} - \Delta N_{1 \to 2}^{\text{Cu}} \cdot \mu_{\text{Cu}} - \Delta N_{1 \to 2}^{\text{In}} \cdot \mu_{\text{In}} - \Delta N_{1 \to 2}^{S} \cdot \mu_{\text{S}} \quad (2)$$

where $\Delta G_{1 \to 2}$ is the free energy difference between reconstructions 1 and 2. In the following, we report the free energy of each reconstruction calculated relative to the stoichiometric surface shown in Figure 1. The upper limit of allowed Cu, In, and S chemical potentials in each slab model is set by the free energy of Cu, In, and S in their most stable bulk phases (i.e., if an atom's chemical potential in the surface is higher than the chemical potential of the atom in a separate phase, then the atom will egress from the surface lattice to form the more stable phase). Here, we consider the formation of pure Cu, In, and S phases, as well as Cu_2S and In_2S_3 phases, which yields the following constraints:

$$\mu_{\text{Cu}} < E_{\text{Cu}}^{\text{bulk}} \quad (3)$$

$$\mu_{\text{In}} < E_{\text{In}}^{\text{bulk}} \quad (4)$$

$$\mu_{\text{S}} < E_{\text{S}}^{\text{bulk}} \quad (5)$$

$$\mu_{\text{Cu}_2\text{S}} = 2\mu_{\text{Cu}} + \mu_{\text{S}} < E_{\text{Cu}_2\text{S}}^{\text{bulk}} \quad (6)$$

$$\mu_{\text{In}_2\text{S}_3} = 2\mu_{\text{In}} + 3\mu_{\text{S}} < E_{\text{In}_2\text{S}_3}^{\text{bulk}} \quad (7)$$

where $E_{\text{Cu}}^{\text{bulk}}$ is free energy of a Cu atom in bulk fcc Cu, $E_{\text{In}}^{\text{bulk}}$ is the free energy of an In atom in bulk tetragonal In, $E_{\text{S}}^{\text{bulk}}$ is the free energy of a S atom in bulk α-S_8,[31] $E_{\text{Cu}_2\text{S}}^{\text{bulk}}$ is the free energy of a Cu_2S formula unit in bulk chalcocite,[32] and $E_{\text{In}_2\text{S}_3}^{\text{bulk}}$ is the free energy of a In_2S_3 formula unit in bulk β-In_2S_3.[33] These reference states were chosen because they are the most stable pure and single-component sulfide phases under ambient conditions;[31−33] the coordinates of each phase are provided in the SI. The chemical potentials of Cu, In, and S atoms in the surface are further constrained by equilibrium with the underlying bulk $CuInS_2$ phase, yielding the relationship:

$$\mu_{\text{Cu}} + \mu_{\text{In}} + 2\mu_{\text{S}} = E_{\text{CuInS}_2}^{\text{bulk}} \quad (8)$$

where $E_{\text{CuInS}_2}^{\text{bulk}}$ is the free energy per formula unit of bulk chalcopyrite $CuInS_2$. To simplify the above free energy relationships, we consider limiting S-rich, Cu-rich, and In-rich cases separately. Assuming S-rich conditions, we set $\mu_{\text{S}} = E_{\text{S}}^{\text{bulk}}$ in eq 5 to obtain the following relationships from eqs 6, 7, and 8, respectively:

$$\mu_{\text{Cu}} < \frac{1}{2}(E_{\text{Cu}_2\text{S}}^{\text{bulk}} - E_{\text{S}}^{\text{bulk}}) \quad (9)$$

$$\mu_{\text{In}} < \frac{1}{2}(E_{\text{In}_2\text{S}_3}^{\text{bulk}} - 3E_{\text{S}}^{\text{bulk}}) \quad (10)$$

$$\mu_{\text{In}} = E_{\text{CuInS}_2}^{\text{bulk}} - 2E_{\text{S}}^{\text{bulk}} - \mu_{\text{Cu}} \quad (11)$$

Using eqs 2 and 11, we plot $\Delta G_{1 \to 2}(\mu_{\text{Cu}})$ for each surface reconstruction subject to upper and lower limits controlled by equilibrium with bulk Cu, In, Cu_2S, and In_2S_3 phases described by eqs 3, 4, 9, and 10, respectively (Figure 4a). Similarly, if we assume In-rich conditions, then we set $\mu_{\text{In}} = E_{\text{In}}^{\text{bulk}}$ in eq 4, yielding the following relationships from eqs 6, 7, and 8, respectively:

$$\mu_{\text{Cu}} < \frac{1}{2}(E_{\text{Cu}_2\text{S}}^{\text{bulk}} - \mu_{\text{S}}) \quad (12)$$

$$E_{\text{In}}^{\text{bulk}} < \frac{1}{2}(E_{\text{In}_2\text{S}_3}^{\text{bulk}} - 3\mu_{\text{S}}) \quad (13)$$

$$\mu_{\text{S}} = \frac{1}{2}(E_{\text{CuInS}_2}^{\text{bulk}} - E_{\text{In}}^{\text{bulk}} - \mu_{\text{Cu}}) \quad (14)$$

Using eqs 2 and 14, we plot $\Delta G_{1 \to 2}(\mu_{\text{Cu}})$ subject to upper and lower limits controlled by equilibrium with bulk Cu, S, Cu_2S, and In_2S_3 phases described by eqs 3, 5, 12, and 13, respectively (Figure 4b). Finally, assuming Cu-rich conditions, we set $\mu_{\text{Cu}} = E_{\text{Cu}}^{\text{bulk}}$ in eq 3 to obtain the following relationships from eqs 6, 7, and 8, respectively:

$$E_{\text{Cu}}^{\text{bulk}} < \frac{1}{2}(E_{\text{Cu}_2\text{S}}^{\text{bulk}} - \mu_{\text{S}}) \quad (15)$$

$$\mu_{\text{In}} < \frac{1}{2}(E_{\text{In}_2\text{S}_3}^{\text{bulk}} - 3\mu_{\text{S}}) \quad (16)$$

$$\mu_{\text{S}} = \frac{1}{2}(E_{\text{CuInS}_2}^{\text{bulk}} - \mu_{\text{In}} - E_{\text{Cu}}^{\text{bulk}}) \quad (17)$$

Using eqs 2 and 17, we plot $\Delta G_{1 \to 2}(\mu_{\text{In}})$ subject to upper and lower limits controlled by equilibrium with bulk In, S, Cu_2S, and In_2S_3 phases described by eqs 4, 5, 15, and 16, respectively. These equations are used to determine an appropriate model of the electrode surface corresponding to varying synthesis approaches and operating environments.

We apply the above equations to establish which reconstructions are most stable under S-rich, Cu-rich, or In-rich conditions (Figure 4). In particular, we are interested in the S-rich limit corresponding to typical electrode synthesis conditions in which a CuIn alloy is exposed to excess sulfur to yield the desired $CuInS_2$ phase.[7,8] The data in Figure 4a demonstrate that, at the S-rich limit, the accessible region of the phase diagram is bracketed by Cu_2S-rich and In_2S_3-rich limits. This process is intuitive, as it will be thermodynamically favored to form separate copper or indium sulfide phases under Cu-rich or In-rich conditions in the presence of excess sulfur. At the In-rich limit, the accessible region of the phase diagram is bracketed by Cu-rich and In_2S_3-rich limits (Figure 4b), as the surface will form a pure copper phase under S-poor/Cu-rich conditions and will form a separate indium sulfide phase under S-rich/In-rich conditions. Analogously, at the Cu-rich limit, the accessible region of the phase diagram is bracketed by In-rich and Cu_2S-rich limits (Figure 4c), where the surface will form a pure indium phase under S-poor/In-rich conditions and will
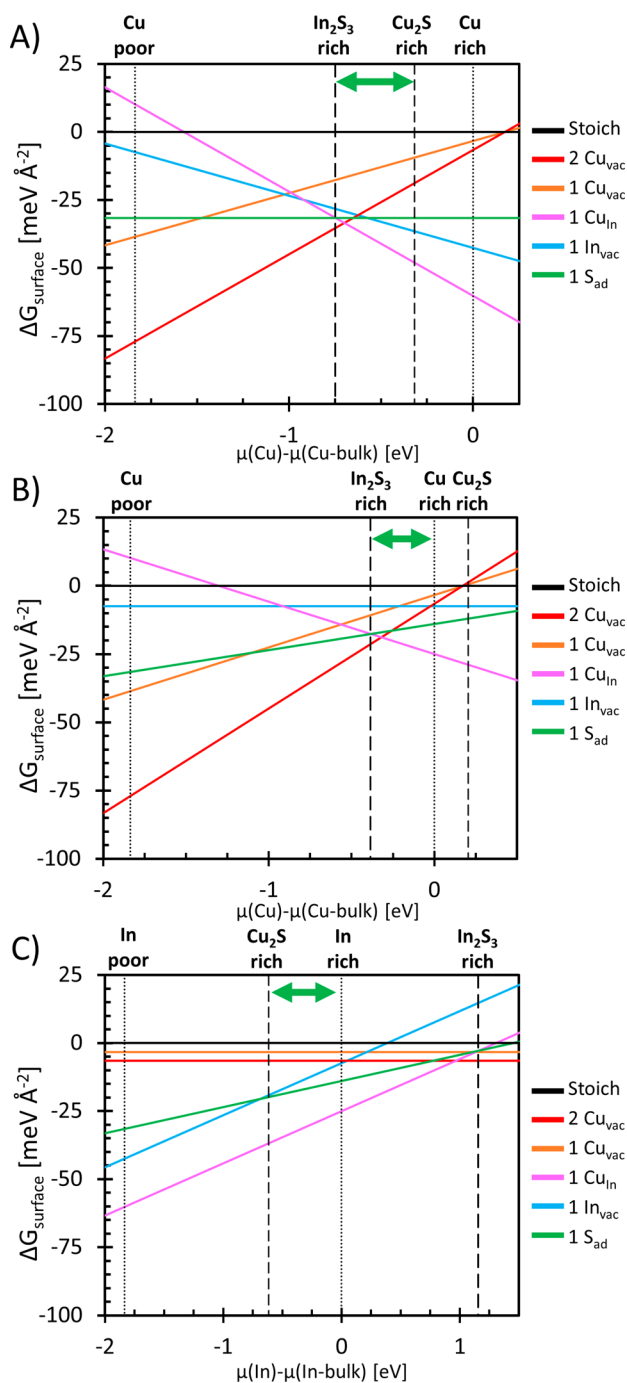
Figure 4. Relative surface free energy, $\Delta G_{surface}$, calculated under (a) S-rich, (b) In-rich, and (c) Cu-rich conditions with a (2×2) unit cell of the CuInS$_2$(112) surface. Green arrows indicate the thermodynamically accessible region of the diagram.

form a separate copper sulfide phase under S-rich/Cu-rich conditions.

As evident at all three limiting conditions, the CuInS$_2$(112)-Cu$_{In}$ reconstruction is thermodynamically stable over most accessible regions of the phase diagram and is particularly stable relative to other reconstructions under Cu-rich/S-rich/In-poor conditions (i.e., toward the right-hand side of Figure 4a). This result corroborates the findings of Jaffe and Zunger[29] and of Zhang and Wei,[30] which both predict that the Cu$_{In}$ reconstruction is thermodynamically favored on the CuInSe$_2$(112) surface. Cu vacancy defects are stabilized

under Cu-poor conditions (i.e., toward the left-hand side of Figure 4a,b), and as such, the CuInS$_2$(112)-2Cu$_{vac}$ surface is thermodynamically favored in these regions. The CuInS$_2$(112)-2Cu$_{vac}$ surface is structurally equivalent to a pure indium sulfide overlayer above a CuInS$_2$ bulk phase (Figure 3d); this surface reconstruction therefore is likely to form just prior to segregation of a separate In$_2$S$_3$ bulk phase, as evident from the position of the In$_2$S$_3$-rich boundary in Figure 4a,b. The CuInS$_2$(112)-1Cu$_{vac}$ surface is never thermodynamically stable because this reconstruction does not satisfy the EC rules discussed in the previous section. Since the CuInS$_2$(112)-2Cu$_{vac}$ will only form when the electrode synthesis is initiated from high In/Cu ratios, we consider the CuInS$_2$(112)-Cu$_{In}$ reconstruction to best represent CuInS$_2$ photoelectrodes synthesized via the sulfurization of ~1:1 CuIn alloys.

CuInS$_2$(112)-In$_{vac}$ and CuInS$_2$(112)-S$_{ad}$ reconstructions, although never thermodynamically favored, are not significantly higher in energy than the CuInS$_2$(112)-Cu$_{In}$ reconstruction under Cu-poor/S-rich conditions. Composition analyses of the CuInS$_2$ electrodes employed by Yuan et al.[8] demonstrated that successful CO$_2$ reduction was only achieved with electrodes synthesized with Cu:In ratios greater than one. The CuInS$_2$(112)-S$_{ad}$ surface features a Cu/In ratio equal to one, and thus we do not consider the CuInS$_2$(112)-S$_{ad}$ surface further in this study since experimental evidence demonstrates that such electrodes are not active. However, both the CuInS$_2$(112)-Cu$_{In}$ and the CuInS$_2$(112)-In$_{vac}$ reconstructions result in Cu:In ratios greater than one, so both surfaces may contribute to the observed activity of the electrode. We consider the formation of mixed reconstructions that feature both In$_{vac}$ and Cu$_{In}$ defects in varying ratios to further investigate the stability of In-vacancy defects (Figure 5). We employ a (4×4)-CuInS$_2$(112) supercell with four surface defects per cell, where we compare the surface free energy of reconstructions varying from all Cu$_{In}$ antisite defects (denoted as (4×4)-0In$_{vac}$/4Cu$_{In}$) to all In$_{vac}$ defects (denoted as (4×4)-4In$_{vac}$/0Cu$_{In}$). The free energy difference between the (4×4)-0In$_{vac}$/4Cu$_{In}$ surface and the (4×4)-1In$_{vac}$/3Cu$_{In}$ surface is 1.88 meV Å^{-2} at the Cu$_2$S-rich limit (i.e., where the formation of In$_{vac}$ defects is least favorable), demonstrating that the formation of In$_{vac}$ defects is energetically feasible. Indeed, the (4×4)-1In$_{vac}$/3Cu$_{In}$ surface is thermodynamically more stable than the (4×4)-0In$_{vac}$/4Cu$_{In}$ surface at the In$_2$S$_3$-rich limit (i.e., where the formation In$_{vac}$ defects is most favorable). We conclude that low concentrations of In$_{vac}$ sites are likely present on the electrode surface, and as such we consider both CuInS$_2$(112)-Cu$_{In}$ and CuInS$_2$(112)-In$_{vac}$ reconstructions in the following sections.

3.2. Impact of Solvation on Band Edge Alignment.
Having determined the most stable reconstructions of the CuInS$_2$(112) surface, we next consider the interaction between the surface and water molecules from the aqueous electrolyte solution. The CuInS$_2$(112)-Cu$_{In}$ reconstruction yields a sp^2 coordination environment surrounding all surface metal sites, leading to empty p states associated with both Cu and In surface atoms. As such, there are no S sites that would expose a lone pair, which is the case on related GaP(111) and CdTe(111) surface reconstructions studied previously.[25] Conversely, such sites are present on the CuInS$_2$(112)-In$_{vac}$ reconstruction, creating exposed lone pair sites that can facilitate the heterolytic dissociation of water. The sp^2-metal and S lone-pair sites are susceptible to multiple donor–acceptor bonding interactions with solvating water molecules.
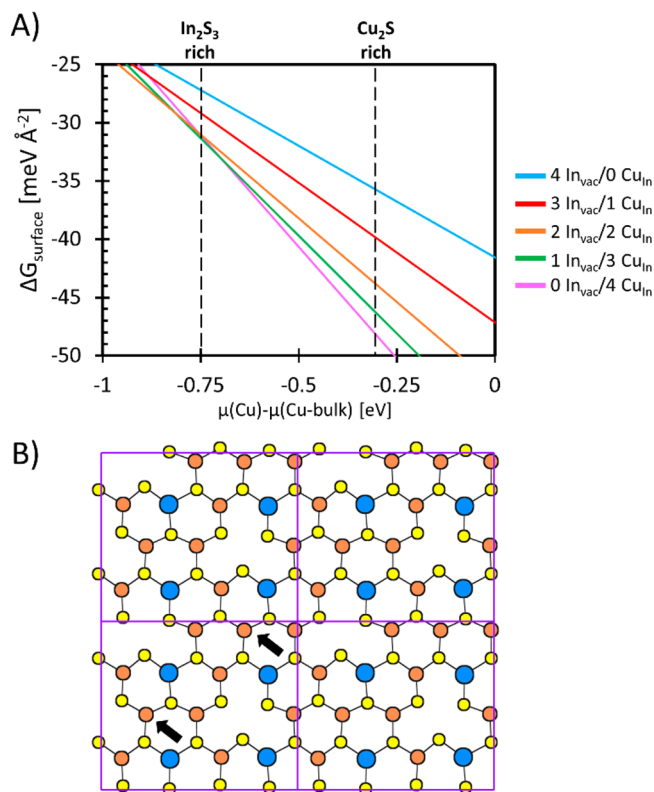
A)

B)

Figure 5. (a) Relative surface free energy, $\Delta G_{surface}$, calculated under S-rich conditions with a (4×4) supercell of the $CuInS_2(112)$ surface. (b) Top view of the optimized (4×4) supercell surface with two In_{vac} defects, and two Cu_{In} antisite defects (indicated by arrows; compare to Figure 2b).

H_2O can adsorb through a O lone-pair interaction at the Cu/In sp^2 sites, or H_2O can heterolytically dissociate and adsorb though a OH^- lone pair dative bond at the sp^2-Cu/In site coupled with a H^+ dative bond at a S lone-pair site (if present). We considered H_2O adsorption and dissociation geometries on both $CuInS_2(112)$-Cu_{In} and $CuInS_2(112)$-In_{vac} surfaces with coverages varying from $\theta = 0.25-2.00$ ML, and with varying degrees of dissociation. A coverage of $\theta = 1.00$ ML is defined as one monolayer with an adsorbed H_2O molecule at every available sp^2 metal site. The 2.00 ML structure was derived by adding a H_2O molecule to form a hydrogen-bond bridge between all H_2O molecules in the 1.00 ML structure (Figure 6). Intermediate-coverage geometries were determined by successively removing high-symmetry H_2O molecules from the ordered $\theta = 2.00$ ML structure (all coordinates are provided in the SI). This approach allowed for a general sampling of many solvent/surface interfacial structures, which was sufficient to derive trends establishing a relationship between band edge position and surface dipoles induced by solvation, as discussed below.

H_2O dissociation is highly unfavorable on the $CuInS_2(112)$-Cu_{In} surface, as there are no exposed lone pairs that can participate in a donor−acceptor bond with a surface proton. We similarly found that dissociation is not favorable on the $CuInS_2(112)$-In_{vac} surface, as the H−S donor−acceptor bond is too weak to promote H_2O dissociation ($\Delta E_{dissociation} = +1.68$ eV). We additionally found that H_2O adsorbs more favorably on In sites compared to Cu sites (e.g., by 0.32 eV at $\theta = 1.00$ ML on the $CuInS_2(112)$-Cu_{In} surface), because the more highly charged surface In^{3+} atom will form a stronger donor−acceptor bond to the H_2O lone pair than the surface Cu^+ atom. Finally, we found that the position of the calculated band gap center (and, therefore, the CBM) is highly dependent on solvation structure and coverage, varying by as much as ∼0.7 eV between low- and high-coverage surfaces (Figure 7). Thus, the most stable surface/solvent coverage must be identified to accurately predict the CBM of the solvated electrode surface.

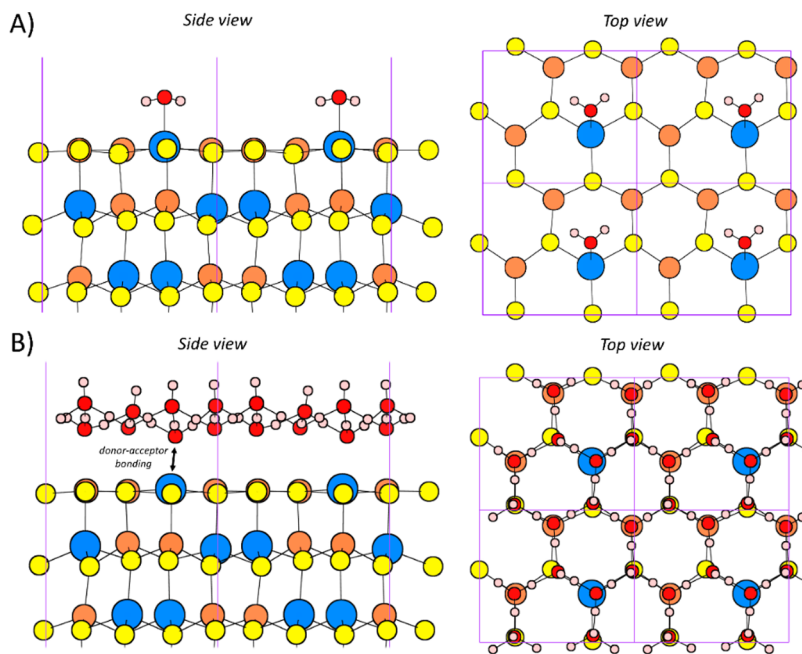We follow the methodology employed in Kronawitter et al.[34] to determine the structures that are the most stable at the

Figure 6. Side and top view of the $CuInS_2(112)$-Cu_{In} surface with a H_2O coverage of (a) $\theta = 0.25$ ML and (b) $\theta = 2.00$ ML. The unit cell is denoted with purple lines, and Cu, In, S, O, or H atoms are represented by orange, blue, yellow, red, or pink circles, respectively.
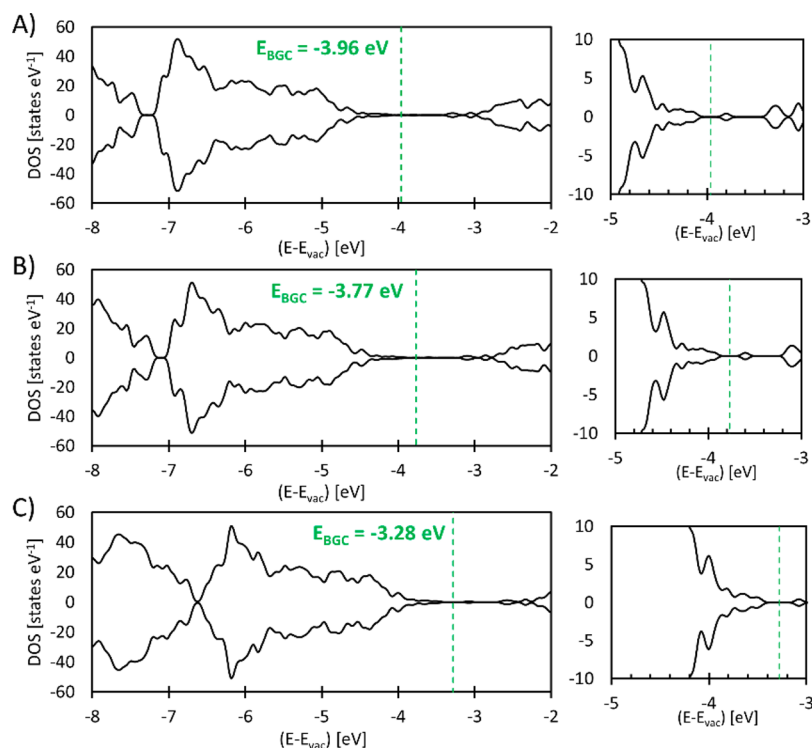
Figure 7. (a–c) Total DOS and band gap center of the $CuInS_2(112)$-Cu_{In} surface at (a) $\theta = 0.25$ ML, (b) $\theta = 0.50$ ML, and (c) $\theta = 1.50$ ML. The vertical dashed line indicates the band gap center.

surface/solvent interface and, therefore, best represent the band edge alignment of the solvated surface. Using the adsorption free energy of H_2O as a function of H_2O chemical potential (Figures 8 and 9), we then follow the methodology established by Toroker et al.[22] to determine E_{BGC} and CBM of each surface/solvent interfacial structure to extract the relationship between band edge position and surface dipole of solvated $CuInS_2(112)$. The reported CBM values are adjusted to match the acidity of the electrolyte employed in the experiments conducted by Yuan et al.[7] (pH = 5.2), using the Nernst relation: $CBM(pH) = CBM(pH_{ZC}) + 0.059 \cdot (pH - pH_{zc})$, where pH is the acidity constant and pH_{zc} is the pH at the point of zero charge. For the $CuInS_2(112)$ surface, we employ the experimentally determined value of $pH_{ZC} = 1.8$.[35,36]

We find that there is a linear relationship between the calculated CBM and the net surface dipole (Figures 8b and 9b). H_2O does not strongly adsorb or dissociate on the $CuInS_2(112)$-Cu_{In} surface, so the most stable H_2O solvation structures tend to minimize the overall surface dipole; water molecules can freely orient themselves to counteract any dipole inherent to the surface in vacuum. This is evident from the lowest energy structures, which cluster near the zero-dipole intercept of the trend-line (Figure 8). The zero-dipole intercept of the CBM vs dipole trend line occurs at CBM = −2.44 eV vs vacuum, which is in good agreement with the experimental value, as reported by Yuan et al.[7] of CBM = −2.64 eV vs vacuum at pH = 5.2. Hence, this approach (i.e., deriving a dipole vs CBM trend-line, and finding the zero-dipole intercept) offers a simple way to approximate the effect of solvation on the band edge positions of a semiconductor surface if the interaction with H_2O is weak (i.e., when there is no adsorption or dissociation that stabilizes a net dipole). This approach assumes that, on average, the dynamic H_2O layer will counterbalance and, therefore, minimize the net surface dipole.

The linear relationship between surface dipole and band gap center is intuitive in this case, as the work function of the slab (calculated directly from the band gap center) will be linearly dependent on the surface dipole because interaction with the dipole will increase or decrease the energy required to remove an electron from the slab (depending on the direction and magnitude of the dipole). Since water interacts weakly with this surface, modification of the surface dipole will represent the most significant contribution to changes in the work function, leading to the direct correlation between dipole and band gap center. This correlation may break down when stronger interactions between the surface and the solution are at play, as demonstrated by Deak et al.[37] for solvated TiO_2 surfaces on which dissociated OH^- and H^+ species adsorb, creating a sustained dipole. Indeed, we find that the In vacancy present in the $CuInS_2(112)$-In_{vac} surface stabilizes a net dipole that systematically shifts all CBM values to lower energies by ∼0.3 eV (e.g., at $\theta = 1.50$ ML the CBM is shifted from −2.42 eV vs vacuum to −2.72 eV vs vacuum, Figure 9). This shift in CBM position results in CBM positions that are generally in better agreement with the value reported by Yuan et al.[7] (CBM = −2.64 eV vs vacuum). This suggests that In_{vac} defects may be present on the $CuInS_2$ electrode employed in their experiments, although this agreement may be fortuitous.

We additionally conducted an AIMD simulation of the solvated $CuInS_2(112)$-Cu_{In} surface to further explore the dipole minimization trend observed in our calculations (Figure 10). The initial geometry for this simulation was built from the most stable structure identified for the solvated $CuInS_2(112)$-Cu_{In} surface, which corresponds to the structure at $\theta = 1.5$ ML water coverage. For this simulation, we chose to double the water coverage by duplicating the water structure at the interface, yielding an equivalent coverage of $\theta = 3.0$ ML. A thicker water layer was chosen to assess how well the above calculations are
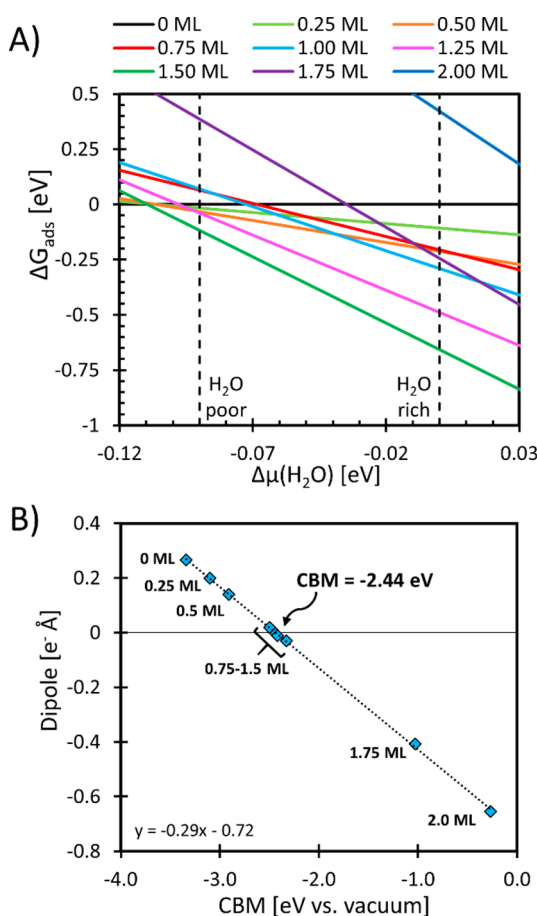
Figure 8. (a) Adsorption free energy (ΔG) of water at the surface/solvent interface of the reconstructed $CuInS_2(112)$-Cu_{In} surface. (b) CBM (at pH = 5.2) plotted against the net surface dipole of the solvated surfaces in (a).

Figure 9. (a) Adsorption free energy (ΔG_{ads}) of water at the surface/solvent interface of the reconstructed $CuInS_2(112)$-In_{vac} surface. (b) CBM (at pH = 5.2) plotted against the net surface dipole of the solvated surfaces in (a).

converged with respect to water layer thickness. The system was equilibrated for 500 fs prior to recording surface dipole data over the course of the 1750 fs simulation (Figure 10). The simulation reveals that the average dipole of the $CuInS_2(112)$-Cu_{In} surface is lowered in the presence of solvating water molecules, as the average surface dipole ($\sim$0.05 e^-Å) is consistently below the dipole of the bare surface (0.27 e^-Å). This confirms that water molecules do not strongly adsorb on the surface, and are therefore free to counter the dipole of the bare surface. This also demonstrates that the dipole minimization trend is not impacted when a thicker solvation layer is employed.

4. CONCLUSIONS

Consideration of surface reconstruction, as well as consideration of interactions with an explicit solvating water layer, is essential for determining the energy of photoexcited electrons originating from a photocathode surface in equilibrium with an electrolyte solution. The polar $CuInS_2(112)$ surface will reconstruct, thus affecting the surface dipole and adsorption sites available to solvating H_2O molecules. We employed DFT +U calculations in conjunction with atomistic thermodynamics to determine stable reconstructions, which predict that $CuInS_2(112)$ will readily form a (2×2) reconstruction with one surface Cu_{In} antisite defect per unit cell. In_{vac} defects are also predicted to be energetically feasible at low concentrations
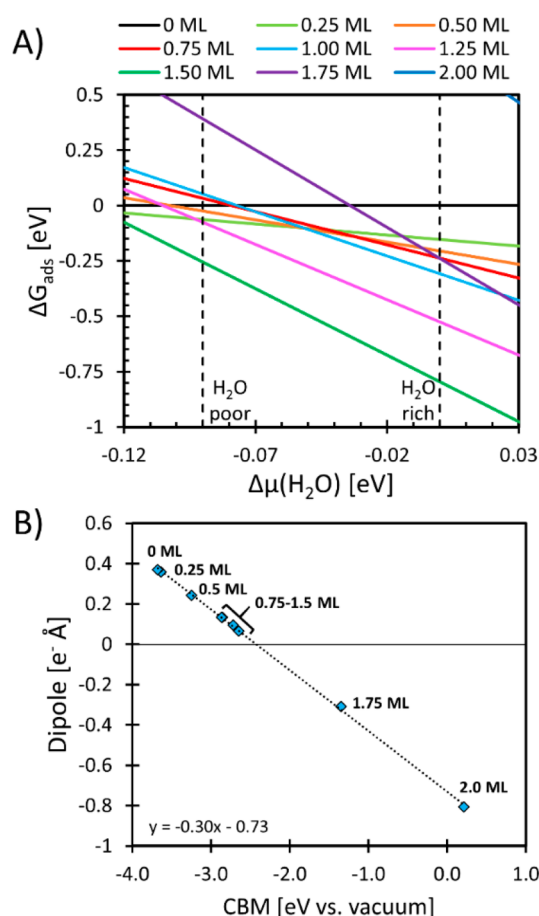
under S-rich/Cu-poor conditions. We found that H_2O molecules interact weakly with the reconstructed $CuInS_2$ surface, where the most stable solvation/surface interfacial structures minimize the net surface dipole. Due to a weak interaction with the surface, the adsorbed water layer will counter the dipole induced by the surface reconstruction. Consideration of multiple water/surface geometries led to the emergence of a linear relationship between the CBM position of the solvated, reconstructed surface and the net surface dipole. This relationship then determined the average CBM position of a solvated surface with zero net dipole. The predicted CBM position (i.e., the CBM at the zero-dipole intercept, −2.44 eV vs vacuum) agrees quite well with the experimentally reported CBM position (−2.64 eV vs vacuum). This methodology therefore offers a simplified approach for predicting the band edge positions of other solvated semiconductor surfaces, without requiring averaging over structures obtained with expensive AIMD simulations. While useful as a first approximation, this approach is limited to situations where water does not strongly adsorb or dissociate, as this can stabilize a net dipole that will affect the band edge positions. As such, the physically relevant structure of other semiconductor/electrolyte interfaces may involve significant dipoles that dictate band edge position.
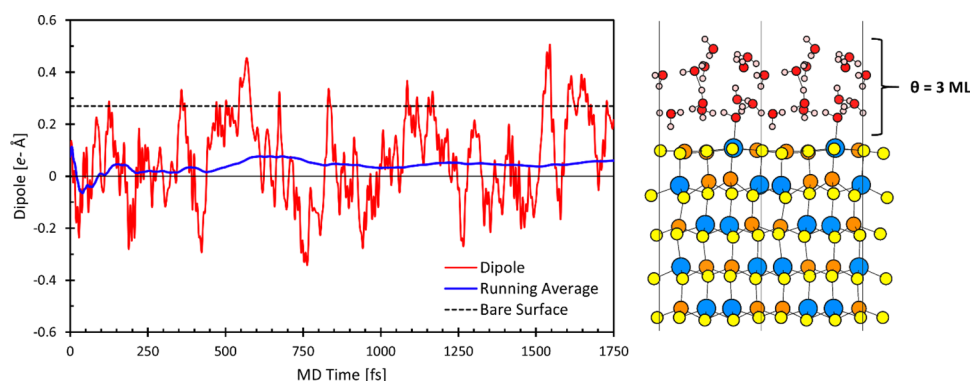
Figure 10. Surface dipole during a 1750 fs AIMD simulation of the dynamic trajectory of water at a coverage of θ = 3 ML over the $CuInS_2$(112)-Cu_{In} surface at 300 K. (Right) Snapshot of the system structure at 1000 fs. The dotted line represents the calculated dipole of the bare $CuInS_2$(112)-Cu_{In} surface (i.e., θ = 0 ML). The instantaneous dipole is shown in red, and the running average of the dipole is shown in blue. Coordinates of the full MD trajectory are available in the Supporting Information.

■ ASSOCIATED CONTENT

Ⓢ Supporting Information

The Supporting Information is available free of charge on the ACS Publications website at DOI: 10.1021/acs.langmuir.7b00668.

> Data showing convergence of the band gap with respect to the number of empty bands and convergence of the band gap center with respect to slab thickness. Atomic coordinates and total DFT + U energies of all stationary-point geometries (PDF).
>
> XYZ file with all structures associated with the AIMD trajectory (XYZ).

■ AUTHOR INFORMATION

Corresponding Author

*E-mail: eac@princeton.edu.

ORCID Ⓘ

Emily A. Carter: 0000-0001-7330-7554

Notes

The authors declare no competing financial interest.

■ ACKNOWLEDGMENTS

■ REFERENCES

(1) White, J. L.; Baruch, M. F.; Pander Iii, J. E.; Hu, Y.; Fortmeyer, I. C.; Park, J. E.; Zhang, T.; Liao, K.; Gu, J.; Yan, Y.; Shaw, T. W.; Abelev, E.; Bocarsly, A. B. Light-Driven Heterogeneous Reduction of Carbon Dioxide: Photocatalysts and Photoelectrodes. *Chem. Rev.* **2015**, *115*, 12888−12935.

(2) Kharche, N.; Muckerman, J. T.; Hybertsen, M. S. First-Principles Approach to Calculating Energy Level Alignment at Aqueous Semiconductor Interfaces. *Phys. Rev. Lett.* **2014**, *113*, 176802.

(3) Cheng, J.; Sprik, M. Alignment of electronic energy levels at electrochemical interfaces. *Phys. Chem. Chem. Phys.* **2012**, *14*, 11245−11267.

(4) Kharche, N.; Hybertsen, M. S.; Muckerman, J. T. Computational investigation of structural and electronic properties of aqueous interfaces of GaN, ZnO, and a GaN/ZnO alloy. *Phys. Chem. Chem. Phys.* **2014**, *16*, 12057−12066.

(5) Pham, T. A.; Lee, D.; Schwegler, E.; Galli, G. Interfacial Effects on the Band Edges of Functionalized Si Surfaces in Liquid Water. *J. Am. Chem. Soc.* **2014**, *136*, 17071−17077.

(6) Pham, T. A.; Ping, Y.; Galli, G. Modelling heterogeneous interfaces for solar water splitting. *Nat. Mater.* **2017**, *16*, 401−408.

(7) Yuan, J.; Hao, C. Solar-driven photoelectrochemical reduction of carbon dioxide to methanol at $CuInS_2$ thin film photocathode. *Sol. Energy Mater. Sol. Cells* **2013**, *108*, 170−174.

(8) Yuan, J.; Zheng, L.; Hao, C. Role of pyridine in photo-electrochemical reduction of CO_2 to methanol at a CuInS2 thin film electrode. *RSC Adv.* **2014**, *4*, 39435−39438.

(9) Yuan, J.; Wang, P.; Hao, C.; Yu, G. Photoelectrochemical reduction of carbon dioxide at $CuInS_2$/graphene hybrid thin film electrode. *Electrochim. Acta* **2016**, *193*, 1−6.

(10) Moll, N.; Kley, A.; Pehlke, E.; Scheffler, M. GaAs equilibrium crystal shape from first principles. *Phys. Rev. B: Condens. Matter Mater. Phys.* **1996**, *54*, 8844−8855.

(11) Kresse, G.; Furthmuller, J. Efficiency of ab-initio total energy calculations for metals and semiconductors using a plane-wave basis set. *Comput. Mater. Sci.* **1996**, *6*, 15−50.

(12) Perdew, J. P.; Burke, K.; Ernzerhof, M. Generalized Gradient Approximation Made Simple. *Phys. Rev. Lett.* **1996**, *77*, 3865−3868.

(13) Dudarev, S. L.; Botton, G. A.; Savrasov, S. Y.; Humphreys, C. J.; Sutton, A. P. Electron-energy-loss spectra and the structural stability of nickel oxide: An LSDA+U study. *Phys. Rev. B: Condens. Matter Mater. Phys.* **1998**, *57*, 1505−1509.

(14) Yu, K.; Carter, E. A. Communication: Comparing ab initio methods of obtaining effective U parameters for closed-shell materials. *J. Chem. Phys.* **2014**, *140*, 121105.

(15) Mosey, N. J.; Liao, P.; Carter, E. A. Rotationally invariant ab initio evaluation of Coulomb and exchange parameters for DFT+U calculations. *J. Chem. Phys.* **2008**, *129*, 014103.

(16) Grimme, S. Semiempirical GGA-type density functional constructed with a long-range dispersion correction. *J. Comput. Chem.* **2006**, *27*, 1787−1799.

(17) Blöchl, P. E. Projector augmented-wave method. *Phys. Rev. B: Condens. Matter Mater. Phys.* **1994**, *50*, 17953−17979.

(18) Kresse, G.; Joubert, D. From ultrasoft pseudopotentials to the projector augmented-wave method. *Phys. Rev. B: Condens. Matter Mater. Phys.* **1999**, *59*, 1758−1775.

(19) Monkhorst, H. J.; Pack, J. D. Special points for Brillouin-zone integrations. *Phys. Rev. B* **1976**, *13*, 5188−5192.

(20) Onida, G.; Reining, L.; Rubio, A. Electronic excitations: density-functional versus many-body Green's-function approaches. *Rev. Mod. Phys.* **2002**, *74*, 601−659.

(21) Heyd, J.; Scuseria, G. E.; Ernzerhof, M. Hybrid functionals based on a screened Coulomb potential. *J. Chem. Phys.* **2003**, *118*, 8207−8215.

(22) Toroker, M. C.; Kanan, D. K.; Alidoust, N.; Isseroff, L. Y.; Liao, P.; Carter, E. A. First principles scheme to evaluate band edge positions in potential transition metal oxide photocatalysts and photoelectrodes. *Phys. Chem. Chem. Phys.* **2011**, *13*, 16644−16654.

(23) Perdew, J. P.; Levy, M. Physical Content of the Exact Kohn-Sham Orbital Energies: Band Gaps and Derivative Discontinuities. *Phys. Rev. Lett.* **1983**, *51*, 1884−1887.

(24) Nikolaj, M.; Yong, X.; Oliver, T. H.; Patrick, R. Stabilization of semiconductor surfaces through bulk dopants. *New J. Phys.* **2013**, *15*, 083009.

(25) Senftle, T. P.; Lessio, M.; Carter, E. A. Interaction of Pyridine and Water with the Reconstructed Surfaces of GaP(111) and CdTe(111) Photoelectrodes: Implications for CO_2 Reduction. *Chem. Mater.* **2016**, *28*, 5799−5810.

(26) Tasker, P. W. The stability of ionic crystal surfaces. *J. Phys. C: Solid State Phys.* **1979**, *12*, 4977.

(27) Pashley, M. D. Electron counting model and its application to island structures on molecular-beam epitaxy grown GaAs(001) and ZnSe(001). *Phys. Rev. B: Condens. Matter Mater. Phys.* **1989**, *40*, 10481−10487.

(28) Chetty, N.; Martin, R. M. Determination of integrals at surfaces using the bulk crystal symmetry. *Phys. Rev. B: Condens. Matter Mater. Phys.* **1991**, *44*, 5568−5571.

(29) Jaffe, J. E.; Zunger, A. Defect-induced nonpolar-to-polar transition at the surface of chalcopyrite semiconductors. *Phys. Rev. B: Condens. Matter Mater. Phys.* **2001**, *64*, 241304.

(30) Zhang, S. B.; Wei, S. H. Reconstruction and energetics of the polar (112) and (−1−1-2) versus the nonpolar (220) surfaces of $CuInSe_2$. *Phys. Rev. B: Condens. Matter Mater. Phys.* **2002**, *65*, 081402.

(31) Rettig, S. J.; Trotter, J. Refinement of the structure of orthorhombic sulfur, α-S8. *Acta Crystallogr., Sect. C: Cryst. Struct. Commun.* **1987**, *43*, 2260−2262.

(32) Evans, H. T. Djurleite ($Cu_{1.94}S$) and Low Chalcocite (Cu_2S): New Crystal Structure Studies. *Science* **1979**, *203*, 356.

(33) Rampersadh, N. S.; Venter, A. M.; Billing, D. G. Rietveld refinement of In2S3 using neutron and X-ray powder diffraction data. *Phys. B* **2004**, *350*, E383−E385.

(34) Kronawitter, C. X.; Lessio, M.; Zhao, P.; Riplinger, C.; Boscoboinik, A.; Starr, D. E.; Sutter, P.; Carter, E. A.; Koel, B. E. Observation of Surface-Bound Negatively Charged Hydride and Hydroxide on GaP(110) in H_2O Environments. *J. Phys. Chem. C* **2015**, *119*, 17762−17772.

(35) Bebie, J.; Schoonen, M. A. A.; Fuhrmann, M.; Strongin, D. R. Surface Charge Development on Transition Metal Sulfides: An Electrokinetic Study. *Geochim. Cosmochim. Acta* **1998**, *62*, 633−642.

(36) Xu, Y.; Schoonen Martin, A. A. The absolute energy positions of conduction and valence bands of selected semiconducting minerals. *Am. Mineral.* **2000**, *85*, 543.

(37) Deák, P.; Kullgren, J.; Aradi, B.; Frauenheim, T.; Kavan, L. Water splitting and the band edge positions of TiO_2. *Electrochim. Acta* **2016**, *199*, 27−34.